MEM vs. FEM: practical crashworthiness insights for macro element modelling applied to sub-assembly and full vehicle automotive structures

Kevin Hughes, João Ramos, Rade Vignjevic, Marek Krzywobłocki, Nenad Djordjevic & James Campbell

Taylor & Francis
Taylor & Francis Group

MEM vs. FEM: practical crashworthiness insights for macro element modelling applied to sub-assembly and full vehicle automotive structures

Kevin Hughes[a] , João Ramos[b], Rade Vignjevic[a], Marek Krzywobłocki[c], Nenad Djordjevic[a] and James Campbell[a]

[a]Centre for the Assessment of Structures and Materials under Extreme Conditions (CASMEC), Brunel University London, Cambridge, UK; [b]Applied Mechanics, c/o School of Aerospace, Transport and Manufacturing, Cranfield University, Beds, UK; [c]Impact Design Europe, Michalowice, Poland

ABSTRACT

This paper proposes a modelling approach for integral vehicle structures, applied to frontal crash loading, based on the Macro element approach. Addressing the idealisation of complex sub-structures and full vehicle was through identification of critical parameters for conversion of validated FEM into MEM equivalents through sensitivity analyses. Two examples of impact onto rigid barriers are presented; 1). Frontal crash energy management system (consisting crush-can and longitudinal engine rail), impacting at 8.6 m/s and 2). A complete vehicle impact at 56 km/hr (15 m/s). Both case studies predict key features of collapse, with force-time histories agreeing within ±10–15% against FEM. Case study 1 required a 3 second solution time versus 1.5 h (8CPUS) mass-scaled FEM (105k element). For Case study 2, MEM required 7.5mins versus 16.5 hrs for a 3 M element FEM vehicle. For all simulations, LS-DYNA R10.0 and Visual Crash Studio R4.0 used. Developing a framework to overcome accuracy/stability problems, together with issues related to robustness and error reduction is discussed. Model complexity was progressive, involving a-priori knowledge of collapse and/or analysing several sub-assemblies to guide idealisation. The level of agreement demonstrates the advantages of MEM as a complementary method to support conceptual vehicle design and offers significant advantages for design exploration, particularly across multiple crash certification cases.

HIGHLIGHTS

- Idealisation of complex sub-structures into Macro element modelling (MEM) equivalents using high fidelity finite element models (FEM)
- Methodology based on critical parameters for conversion of validated FEM into MEM
- Proposed MEM conversion for complete vehicle frontal impact onto a rigid barrier
- Correlation of critical parameters with structural behaviour through sensitivity analyses
- MEM error in force-time histories within 10–15%, relative to high fidelity FEM
- FEM Solution times reduced from several hours to several minutes for MEM equivalents

1. Introduction

When modelling dynamic collapse of thin-walled structures, explicit finite element codes with an appropriate (converged) high fidelity model are routinely used. As computational power increases through SMP and MPP architectures, so too does modelling complexity. For automotive applications, predicting failure in joints/fasteners [1], or inclusion of residual stresses and geometric thinning in stamped parts [2], requires long simulation times due to accurate geometric representation, appropriate constitutive and damage laws (to account for stress triaxiality and non-local failure criterions [3,4]).

To support the early design phase, the Macro Element Method (MEM) was developed to predict thin-walled dynamic collapse. Through Wierzbicki and Abramowicz (Table 1), its main advantage over traditional finite elements

is significant reduction in computational cost due to calculations performed at the cross-sectional level, allowing MEM analyses to be completed in minutes, versus several hours using parallelised explicit FE solvers. Applications include comparing accuracy of MEM for 3D spaceframes, focussing on joint collapse for A and B pillars, front side members and a rear frame component for different collapse conditions [12], full vehicle crash [13] and more recently, coupling MEM with evolutionary algorithms to optimise a vehicle frontal rail [14].

This paper represents the next step in the development of the basic MEM concepts proposed by Georgiou [13]. Instead of Georgiou's proposition for 'trial and error simulations need to be run in order to identify the triggering forces of the crush boxes that match the collapse modes', this paper develops a structured approach based on critical

Table 1. Chronological summary of key developments in the Macro Element Method (MEM).

Date	Author	Key developments
1960	Alexander [5]	Approximated concertina deformation by repeated shape functions and developed an expression to predict the energy dissipated in three, stationary circumferential plastic hinges during the crushing of a single lobe.
1983	Abramowicz [6]	Modified Alexander's calculations for effective crush depth by incorporating the effect of material strain hardening
1984	Abramowicz [7]	Addressed underestimation in Kinetic Energy for square tubes under axial collapse by introducing a correction for effective crush distance to allow for mixed mode asymmetric collapse.
1986	Abramowicz and Jones [8]	Experimentally validated effective crushing distance concept and developed semi-empirical formulations to describe symmetric and asymmetric collapse in circular and square tubes under dynamic loads
1986	Wierzbicki and Bhat [9]	Modified Alexander's solution by replacing stationary plastic hinges, with moving hinges and led to improved prediction of mean crush force.
1994	Wierzbicki et al [10], [11]	Introduced a transition zone model (the basis for superfolding elements) to reproduce qualitatively and quantitatively the main features of collapse. Compared cross-section stress profiles with FEM and demonstrated MEM was an effective method for thin-walled collapse under axial compression, bending and combined bend-compression loading.

parameters and sensitivity studies to address these issues. This was applied to detailed idealisation of complex sub-structures used in simulation for frontal crash to illustrate robustness and accuracy of the MEM approach. For all simulations, FEM and MEM results were generated by LS-DYNA R10.0 [15] and Visual Crash Studio R4.0 [16]:

1. Frontal crash energy management system (consisting crush can and longitudinal engine rail) onto a rigid barrier at 8.6m/s, whereby MEM accuracy assessed against an OEM validated, high-fidelity FEM element model, in terms of collapse sequence and force-time histories.
2. Complete vehicle impacting at 56km/hr (15m/s) onto a full barrier and compared against high-fidelity FEM. Three MEM variants were considered to assess influence of wheels and auxiliary systems (cooling pack) on crash response.

This paper reviews the MEM approach and highlights key differences to FEM, through investigating its capabilities (and limitations) in predicting axial collapse. The paper concludes with a framework to minimise errors and practical insights for MEM modelling of complex automotive structures.

2. The macro element method (MEM) and role of superfolding beam elements (SBE)

Detailed theory behind the Macro Element Method can be found in the literature [17,18]. In summary, this method is based on the concept of a Super Folding Element (SFE) at the cross-section level and Super Beam Elements (SBE) for 3D structures. The approach uses a kinematic method of plasticity and energy method of classic elasticity to predict localised plastic collapse after the onset of elastic, or elasto-plastic buckling.

An SBE is formed from a series of SFE, whose length is related to the plastic folding wave for repeating hinge patterns (2H), based on five possible collapse mechanisms along a single corner line in a prismatic tube (Figure 1). As each SBE has two deformable sections, the smallest

recommended discretisation length is equal to 4H (i.e. two plastic folding waves) and should not be smaller than the minimum plastic folding wave. This approach is based on Kirchhoff–Love theory (i.e. cross-sections during deformation remain perpendicular to deforming centroid line).

The nomenclature and basic geometric definition of a SFE using four parameters is presented in Figure 1, where, a and b are the dimensions of the two arms of a SFE; Total Length, $C = a + b$; Φ is the central angle and t_a and t_b are the wall thicknesses of both arms a and b respectively. A switching parameter, α^*, which is a function of $\{C, \Phi, t\}$, defines the change in rotation of an initially vertical side face, allowing symmetric, asymmetric and mixed modes of deformation.

The Macro Element Method only requires information at the cross-sectional level (to calculate axial, bending and torsional collapse responses), together with nodal positions for each element. As this paper only deals with axial collapse, the key equations in Table 2 are summarised from [17–19].

For kinematically admissible deformations, equation 1 depends upon three geometric parameters; average rolling radius (r), plastic folding wave length (2H), and switch parameter α^*, which influences the level of tensile deformation in conical surface 4 (Figure 1). These parameters are determined by minimising the expression for the mean axial crush force for a single hinge:

$$P_m = \frac{t^2}{4}\left\{\sigma_0{}^N(\overline{\varepsilon_1})A_1\frac{r}{t} + \sigma_0{}^M(\overline{\varepsilon_2})A_2\frac{C}{H}\frac{1}{H} + \sigma_0{}^M(\overline{\varepsilon_3})A_3\frac{H}{r} + \sigma_0{}^M(\overline{\varepsilon_4})A_4\frac{H}{t} + \sigma_0{}^N(\overline{\varepsilon_5})A_5\right\}\frac{2H}{\delta_{eff}}$$

(4)

Where σ_0^N and σ_0^M are equivalent stresses from uniaxial tension/compression and bending respectively; $\overline{\varepsilon_i}$ are the corresponding strain measures, A_i terms are a function of (Φ, α^*) and represent the fractional contributions from the five deformation mechanisms in Figure 1 and δ_{eff} is the effective crush distance.

The instantaneous axial crushing force is obtained by summing the fractional contributions of all active super folding elements, and equating the rate of external loading, $\dot{E}_{ext} = P(\delta)\dot{\delta}$, to the rate of internal energy dissipation
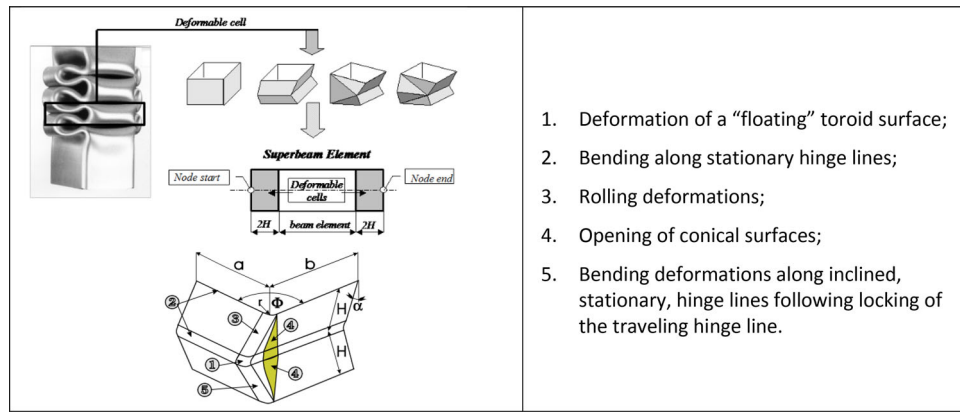
Figure 1. (a) Crushing response of a single layer of folds in a SBE [11] and b) The five plastic folding deformation mechanisms at a single corner in a prismatic tube [19].

Table 2. Key equations for determining axial, bending and torsion collapse for a cross-section [18].

Axial collapse determined for all kinematically admissible deformation histories, $\bar{h}$, (which includes loading, reloading and reverse loading processes), using the rate of internal energy dissipation, $\dot{E}_{int}$	$\dot{E}_{int} = \int_S N_0 \dot{\varepsilon}_1 dS + \sum_{i=1}^{n} \int_{L^i} M_0^i \left[\dot{\theta}_i\right] dl^i (1)$ where N_0 is the fully plastic membrane force; $\dot{\varepsilon}_1$ corresponds to the rate of deformation; S is the continuous deformation fields corresponding to toroidal and conical surfaces 1 and 4 in Figure 1; M_0 is the fully plastic membrane bending moment; L^i is the length of the plastic hinge line; and $\left[\dot{\theta}_i\right]$ is the jump function associated with each hinge line discontinuity of angular velocity.
Bending (M) and torsion moments (T) for all kinematically admissible deformation histories, $\bar{h}$, obtained by analysing stress distribution at the boundary of each deformable cell and integrating along length of cross-section:	$M(\theta, \dot{\theta}, \bar{h}) = \int_L \sigma(\theta, \dot{\theta}, \bar{h}, l) dl (2)$ $T(\gamma, \dot{\gamma}, \bar{h}) = \int_L \tau(\gamma, \dot{\gamma}, \bar{h}, l) dl (3)$

(where $\dot{\delta}$ is the rate of axial crushing and $\bar{h}$ is the deformation history):

$$P(\delta, \dot{\delta}, \bar{h}) = \frac{\dot{E}}{\dot{\delta}} \qquad (5)$$

Knowing the collapse properties for each cross-section, this information defines an interaction surface, which for each deformation step, allows distinction between elastic, limit load, post collapse and deep collapse regimes, based upon the deformation history and current rate of deformation (through cross-sectional forces):

$$\left(\frac{P}{P_{max}}\right)^{a1} + \left(\frac{M_y}{M_{ymax}}\right)^{a2} + \left(\frac{M_z}{M_{zmax}}\right)^{a3} + \left(\frac{T}{T_{max}}\right)^{a4} = 1 \qquad (6)$$

Where P_{max}, M_{ymax}, M_{zmax}, T_{max} are the maximum values for the crushing characteristics, a_i are constants based on the initial geometry, material properties and deformation history defined for each cross section.

To solve the equation of motion, $[M]\{\ddot{u}\} = \{f_{int}\} - \{f_{ext}\}$, where [M] is the mass matrix, u is the displacement vector, $\{f_{ext}\}$, is the vector of applied external and body forces, and $\{f_{int}\}$, is the vector of internal loads, MEM uses an object orientated approach (Figure 2). This greatly simplifies implementation by decoupling node and element calculations, requiring only four entities:

1. Nodes, which govern global equilibrium of the model;

2. Elements, which impose loading onto nodes as a result of motion of other nodes;
3. 'Interface' objects, performing communication between nodes and elements;
4. 'Iterator' objects, responsible for time integration routine.

This decoupling is the key difference between MEM and FEM, as once the internal force vector is determined, MEM does not require information about the number of elements linked to a particular node. Therefore, each iteration step is governed by global equilibrium and executed on node-by-node approach, whilst the update of the structure (i.e. constitutive update, contact, etc.) are performed on an element-by-element basis and communicated only with nodes *via* interface objects. This means the particulars of an element are not visible at the node level and so does not affect global assembly, or time integration (Table 3) [20].

3. Capabilities of MEM in predicting axial tube collapse

Following Witteman, an initial study compared both approaches for various (symmetrical) cross-sectional tubes under axial collapse [21]. Each tube was manufactured from a cold rolled low carbon steel, 350 mm in length with a uniform 2 mm wall thickness and represented by a tabulated flow stress-plastic strain curve, where strain rate effects were accounted through the Cowper–Symonds equation (Figure 3). Material failure was not considered and mass per unit
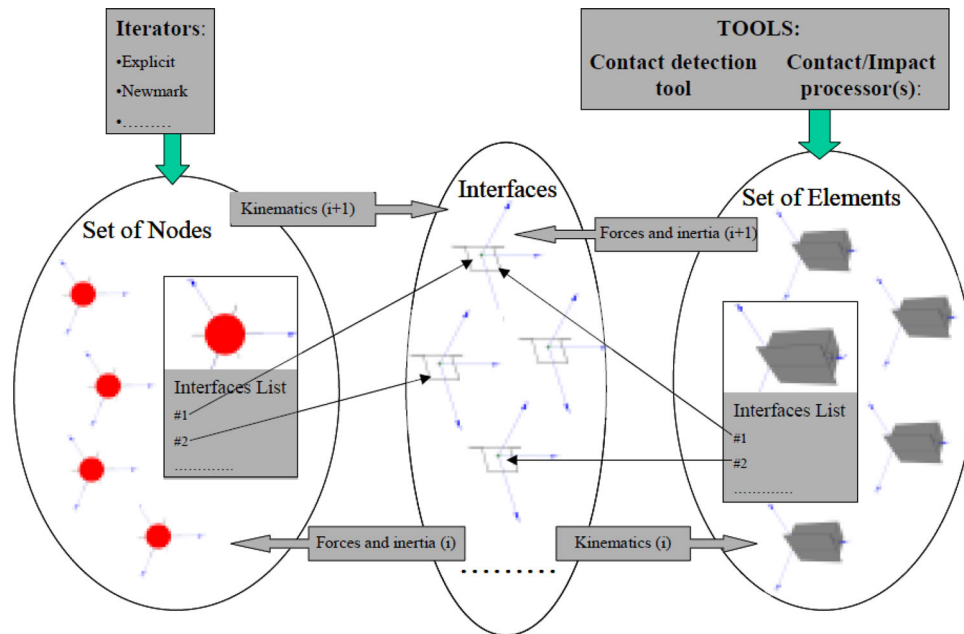
Figure 2. Schematic representation of the solution process where node and element calculations are decoupled through interface objects [20].

Table 3. Explicit time stepping routine implemented in the Macro Element Method [20].

Operations on Nodes:
1. Obtain forces and moments from interfaces and calculate reduced forces and moments
2. Compute accelerations
3. Update nodal velocities
4. Enforce essential boundary conditions for predefined set of nodes
5. Update nodal displacements and orientation
6. Update kinematic variables at connected interfaces
7. Write output for nodes
Operations on Elements:
1. Get kinematic variables from interfaces connected to the element
2. Update the state of elements
3. Compute measures of deformation and resulting forces. Compute inertia properties (typically once per $10^2 - 103$ iteration steps)
4. Set forces and inertia on connected interfaces
5. Write output data for elements
6. Go to the next iteration step

length for each tube was kept constant by maintaining a constant perimeter length (300 mm).

Each tube was encastre, with loading applied through a rigid wall moving at constant velocity (56 km/h) and constrained to only allow uniaxial translation. Contact friction and triggers were not considered and default element types assigned. MEM used a single Super Beam Element (SBE) initially, whereas mesh convergence required a 2 mm element size for square, rectangular and circular cross-sections and a finer 1 mm mesh for hexagon and octagon cross-sections.

Bottoming out effects were avoided by analysing 220 mm of collapse (∼60% of tube length). As only a single SBE was used, collapse was represented by a single state only (i.e. deep collapse = red in colour), whereas FEM differentiates deformed and undeformed regions (Figure 3):

- The rectangular cross section does not exhibit a uniform asymmetrical mode of collapse;

- The circular cross section changes from efficient concertina folding to diamond shape, with a corresponding loss in energy absorption capacity;
- The octagon presents a mixture of circular and diamond symmetric hinge modes, together with an additional hinge forming at the opposite end;
- Square and hexagonal tubes present asymmetrical and symmetrical hinges respectively;

Collapse force and internal energy, as a function of axial tube deformation are presented in Figures 4 and 5. With only one SBE, good correlation is found for square and rectangular cross sections (i.e. <8% difference). However, circular, hexagon and octagonal profiles overestimated the energy absorbed by +29.3%, +21.1% and +59% respectively (Table 4).

MEM Peak collapse force were ∼45 to 55% larger when compared to FEM, with mean collapse force comparable for square and rectangular cross-sections, but overestimated for circular (+37%), hexagonal (+28%) and octagonal (+48%) sections. Evolution of successive plastic hinges were uniform for MEM (Figure 4).

Comparing number of hinges formed, simple cross sections agree with FEM, but overestimated for hexagonal and octagonal cross-sections (Table 5). These differences are attributed to contact in FEM (and also related to element size and formulation) influencing the deformed shape for more complex sections (see inset image, Figure 4), whereas progressive folding is based upon plastic buckling and von-Karman effective width theory (and more conservative).

3.1. Influence of SBE discretisation

As the minimum plastic folding wave (2H) determines the recommended minimum SBE length (4H), discretisation was investigated for rectangular and octagonal sections only,
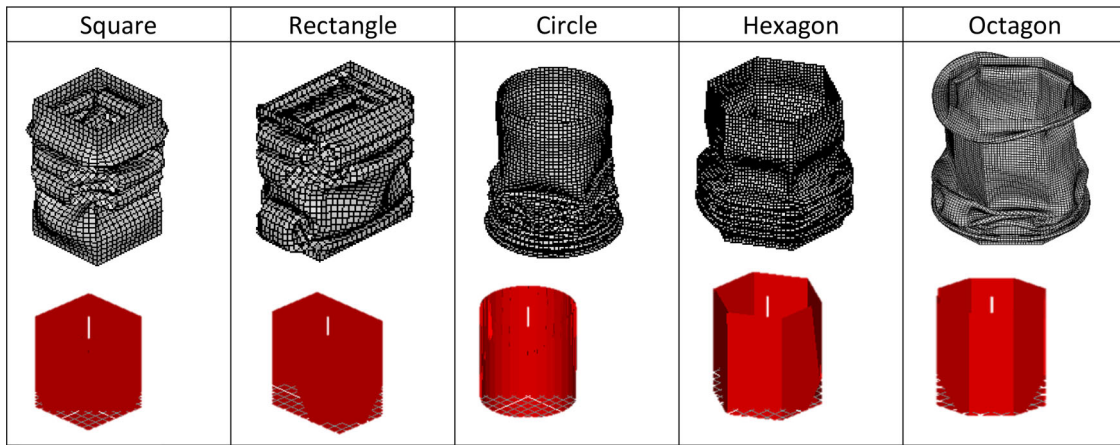
Figure 3. Comparison between MEM and FEM axial collapse (220 mm stroke) for varying cross-sections.
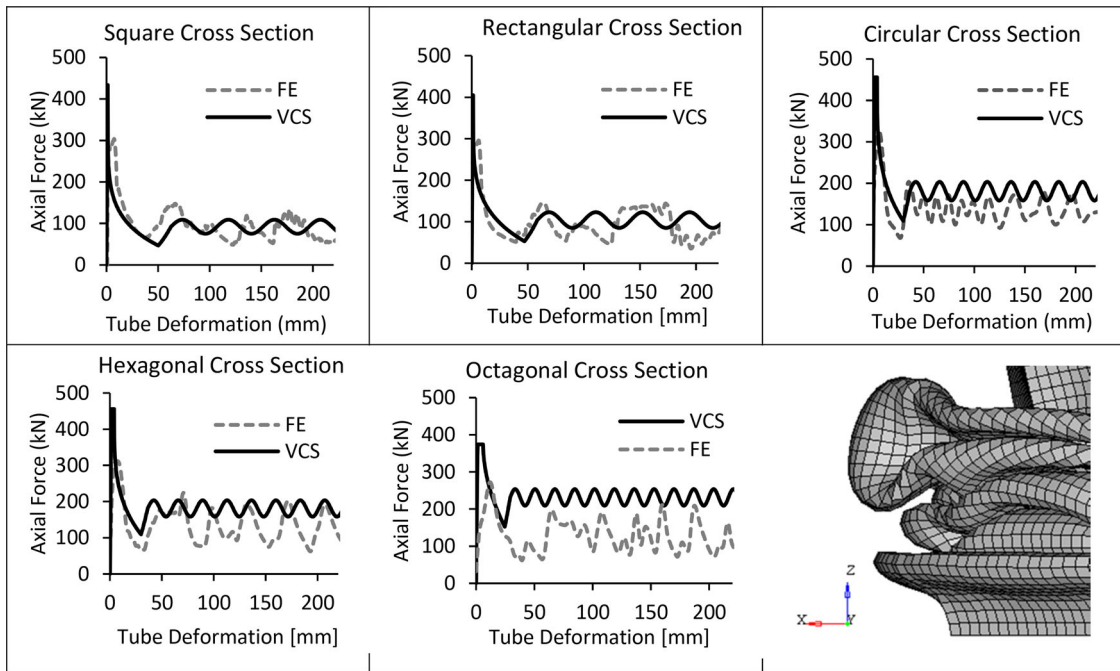

Figure 4. Force-Deflection results for FEM and MEM (VCS) for five different cross-sections. Lower right image shows the post collapse shape for the octagonal cross-section.
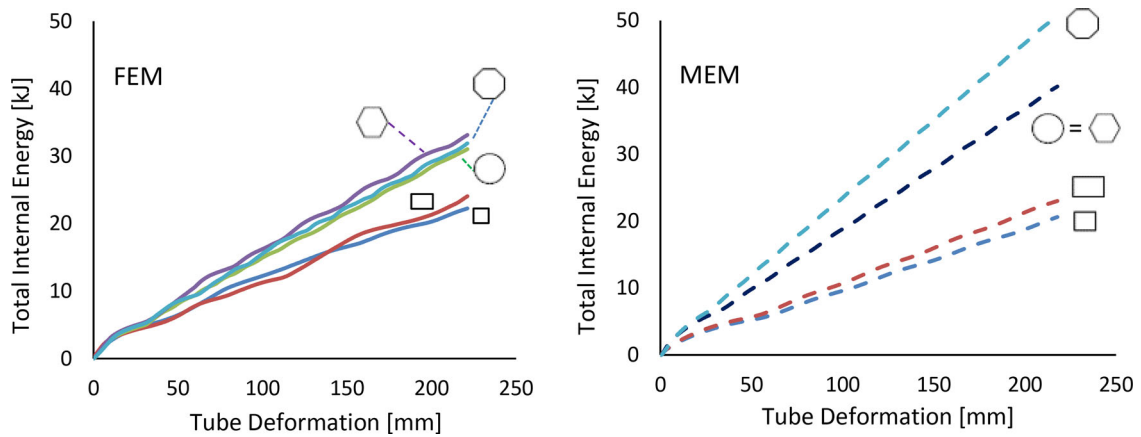

Figure 5. Internal Energy predicted by FEM and MEM for five different cross-sections under axial collapse.

in terms of energy absorbed and axial force. Figure 6 compares one, three and seven SBE (i.e. ∼minimum length for octagonal section, Table 5).

Table 4. Comparison between Internal Energy calculated by FEM and MEM for five different cross-sections.

Profile	FE: Internal Energy (kJ)	MEM: Internal Energy (kJ)	% Error (MEM/FE)
Square	22.25	20.64	−7.2
Rectangle	24.07	23.03	−4.3
Circle	31.04	40.15	+29.3
Hexagon	33.15	40.14	+21.1
Octagon	31.91	50.74	+59.0

Table 5. Number of hinges predicted by MEM and FEM for axial collapse of tubes with varying cross-sections.

	FEM	MEM	
Tube	Number of folds	Number of Folds	Minimum plastic wave* (mm)
Square	4	4	61.06
Rectangle	4	4	32.25
Circle	8	8	32.25
Hexagon	6	8	57.18
Octagon	7	11	26.09
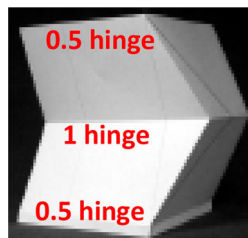
.
*- Minimum plastic wave is the definition of a single folding mechanism).
(0.5 + 1 + 0.5 = 2 hinges in total).

For internal energy, increasing SBE elements reduced discrepancy between MEM and FEM (Figure 6). Convergence achieved using one or three SBE for rectangular section, whereas for the octagonal section, the internal energy reduced from 50.7 J (1SBE) to 37.6 J (7SBE), which was still ∼22% larger than FEM (29.1 J). In terms of force (Figure 6b and c), increasing SBE resulted in additional force peaks; a consequence of increasing the rigid interfaces at each SBE connection. During collapse, once the stroke in one SBE was utilised, the structural stiffness increases until collapse initiates in a subsequent SBE (and so on), which may overestimate mean crush force (and energy absorbed).

Visually comparing post collapse geometry (Table 6), the multi SBE representation for the rectangular section appears closer to FEM, as plastic deformation (deep collapse) at both ends of the tube predicted. For octagonal, seven SBEs predicted deep collapse at the base of the tube, but was unable to predict the hinge predicted by FEM at the loaded end. Therefore, visual indicators of collapse in multi-SBE models should be viewed with caution and may be misleading.

4. High fidelity FEM: Automotive frontal crash management system

The longitudinal engine rail forms part of the frontal crash management system (CMS) of a modern integral vehicle. Comprising four main components: front armature, a multi-celled crush can, a (substantial) casting and longitudinal assembly (), this OEM crash structure was designed to collapse at 130 kN at 8.6 m/s and absorb ∼28 kJ.

Consisting 68 individual parts, including bolts, spotwelds and fillet welds (with heat affected zone properties), the mass was 4.6 kg and contained 105.5k elements (Figure 7).
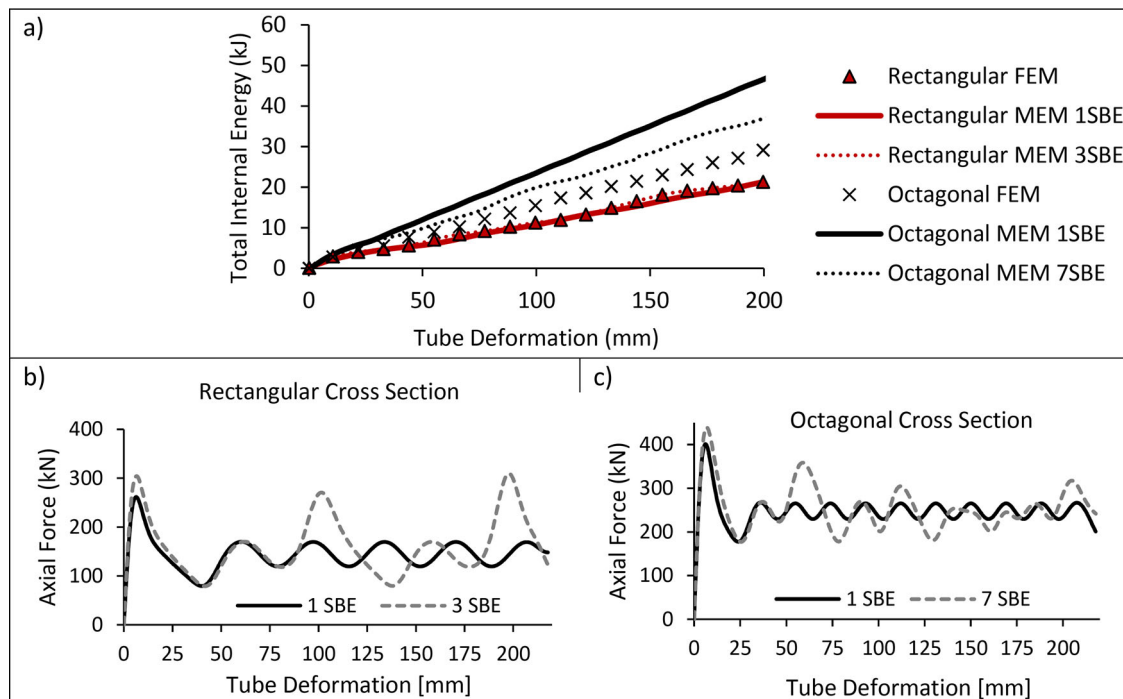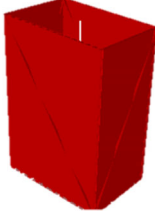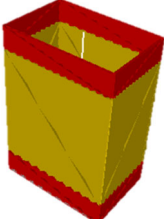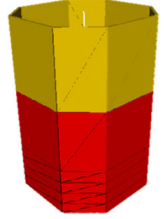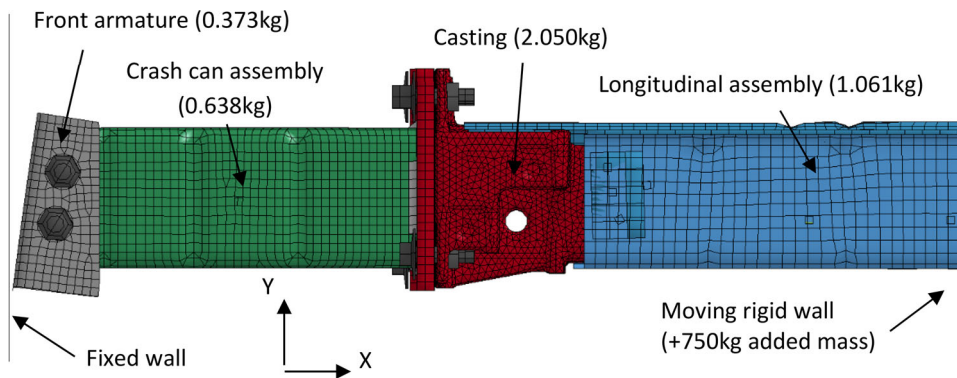

Figure 6. (a) Influence of the number of SBE on total internal strain energy and axial collapse force for MEM (b) rectangular, and (c) octagonal sections.

Table 6. Comparison between FEM and MEM as a function of the number of SBE (yellow and red denotes post and deep collapse respectively).

Profile	FE Model	Single SBE Model	Multi SBE Model
Rectangle			
Octagon			

Figure 7. Side profile of the frontal Crash Energy Management System.

Table 7. Nominal material properties represented by a linear piecewise plasticity model.

Component	Material	Nominal Properties
Front Armature	Steel	σ_Y =700MPa, UTS = 880MPa, Failure Strain ∼9%
Crush Can	Aluminium	σ_Y=252MPa, UTS = 335MPa, Failure Strain ∼ 12%
Back plate	Aluminium	σ_Y =260MPa, UTS = 400MPa, Failure Strain ∼10%
Casting	Aluminium	σ_Y =175MPa, UTS = 300MPa, Failure Strain ∼15%
Longitudinal Assembly	Aluminium	σ_Y =209MPa, UTS = 330MPa, Failure Strain ∼15%

Loading was applied at the rear of the longitudinal assembly through a moving rigid wall, to which half the projected car mass (750 kg) was added. Taking the components from left to right (), with nominal properties defined in Table 7:

- Front armature forms the initial contact point and due to its 8° canted geometry, lowers Peak Crush Force (PCF) by locally loading the section axially and in bending. Armature side walls are attached via four bolts to crush can, constrain plastic hinge expansion (right image, Figure 8).
- With outer dimensions (79.8 by 112.4mm), the multi-cell crush can consists two rectangular sections divided by a central horizontal rib, welded to a backing plate. Constructed from aluminium, three trigger pairs promote stable and progressive collapse. Based on design recommendations for favourable folding, the design satisfied section aspect ratio (d/b) and thickness to breadth (t/b) ratios [22,23].
- The casting forms a substantial connection between crush can back plate (via bolted connections) and longitudinal rail.
- Longitudinal rail is a closed top-hat section (Figure 9), designed to withstand greater collapse loads through local sidewall reinforcements (welded plates) and multiple, staggered triggers.

FEM validation focused on crush can collapse and densification (as controls loading imparted to the longitudinal assembly). Qualitative comparison captured main collapse features (Figure 10), in addition to axial shortening within 1%; ∼326 mm (FEM) vs ∼329 mm (Test).
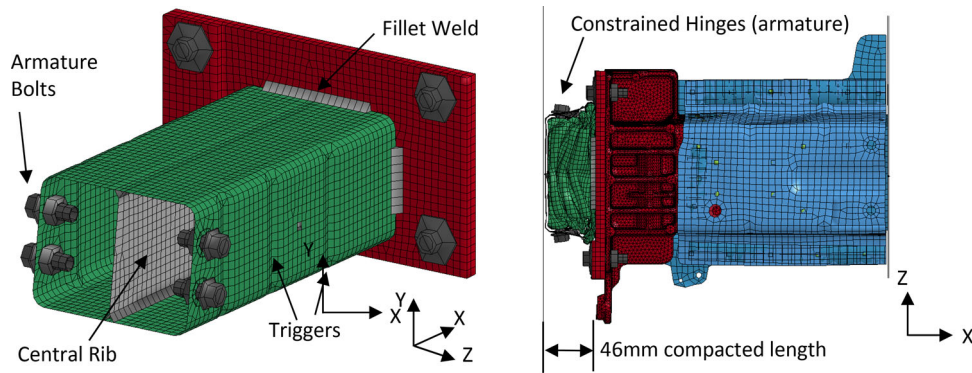
Figure 8. Crush can (left) and deformed armature and crush can assembly (right) after 28 ms.
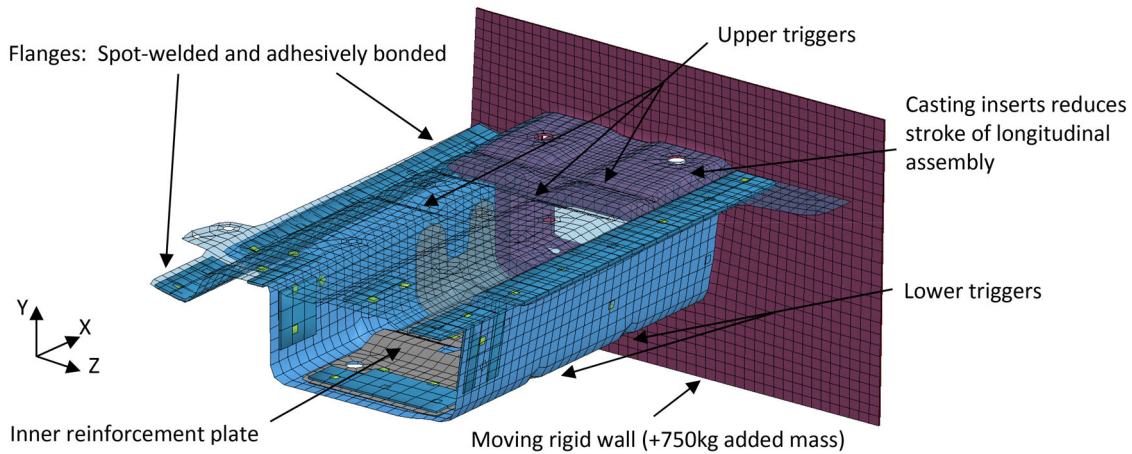

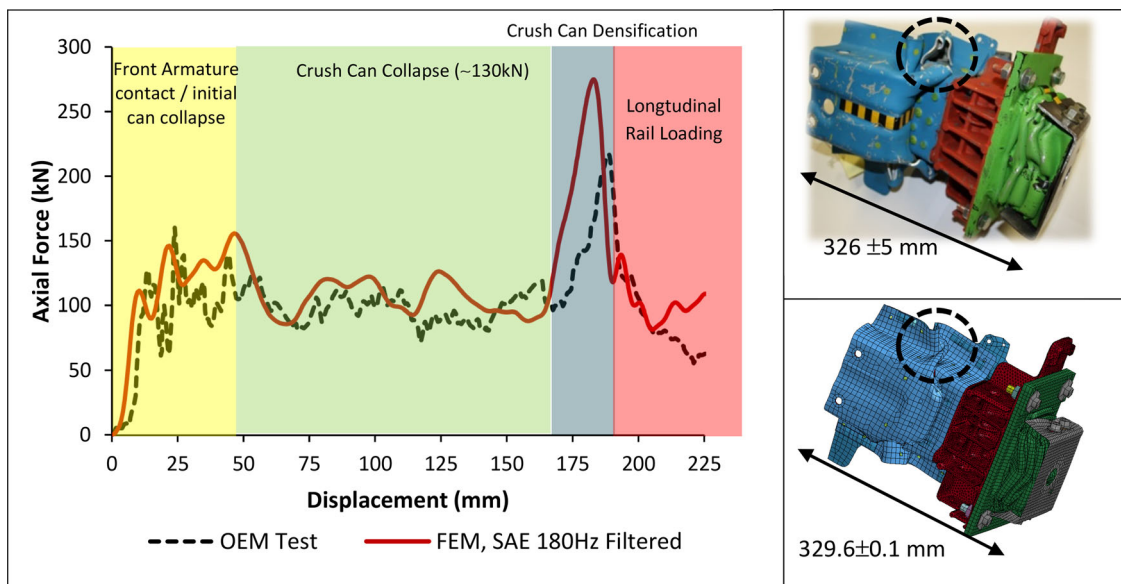**Figure 9.** Longitudinal Rail Assembly (Note: Upper surface has been made transparent).

Figure 10. Crush can validation for an 8.6 m/s impact onto a rigid barrier. Inset images show axial shortening, where test specimen measurement obtained using ImageJ processing software [24].

Good agreement obtained for initial and mean collapse force (Figure 10), with a peak of ~154 kN reducing to ~130 kN (mean) design requirement after trigger activation. The second peak corresponds to crush can densification (FE: ~166 mm vs test: ~172 mm stroke), resulting in longitudinal rail collapse along a single, dominant hinge. FEM overestimates the magnitude and stiffness of this peak, as ductile tearing (circled) was not predicted due to simplified failure criterion used. As predicting ductile failure was not the intention of this analysis, the high-fidelity FEM was considered representative of the real structure to allow assessment of the Macro-element method.
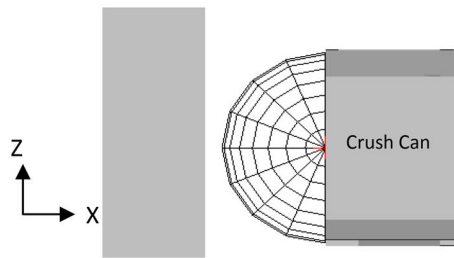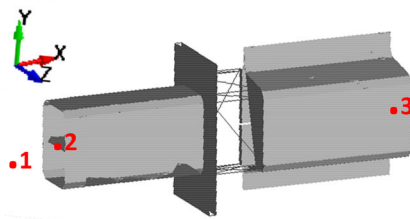
Contact Coefficients	
Friction coefficient	0.80
Restitution coefficient	0.01
Stiffness coefficient	1.00

Figure 11. Definition of contact between rigid barrier and outer crush can SBE.

Node	V_x	W_x	V_y	W_y	V_z	W_z
Wall Node: #1	Fixed		All Fixed			
Front Crush Can Node: #2	8.6 m/s		All Fixed			
Rear (Longit) Node: #3	8.6 m/s		All Fixed (750kg applied)			
Remaining Nodes	8.6 m/s		Free			

Figure 12. MEM Boundary conditions (V_i/W_i = translational/rotational velocity components respectively).

5. Baseline MEM approach: Initial response

MEM does not offer the full range of material types, boundary conditions and connections available within a commercial FEM code. Therefore, this section discusses simplifications/assumptions required for each structural component to develop a MEM equivalent.

5.1. Front armature/crush can

The cross-section was approximated by eight points and as triggers applied at the cross-sectional level through (hoop) dents, four SBE represented the three triggering pairs. As the front armature did not deform (but provides a trigger and constraint to plastic hinge formation), this complexity was neglected, but represented through a user-defined triggering dent of 3.78 mm (vs 2.9 mm in FEM), to meet the 130 kN mean collapse force design requirement (P_m=137.6 kN).

5.2. Back plate and casting

For load transfer, analytical rigid entities were assigned to components not undergoing deformation.

5.3. Longitudinal assembly

Approximated as a wide trapezoid consisting of two plates, assumed to be continuously welded along its length, as spot weld pitch (and failure) are not implemented. Key consideration is alignment of crush stroke to the real structure. With the casting (and end connections) inserted within the rail (Figure 9), the MEM rail was shortened to remove influence of end reinforcements.
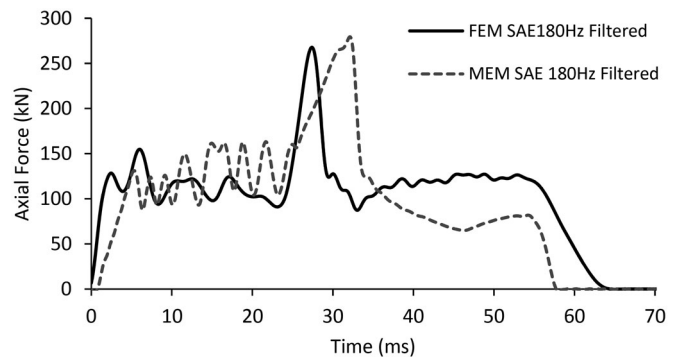

Figure 13. Baseline filtered Force-Time comparison between MEM and FEM (SAE 180 Hz).

5.4. Impact barrier and contact

The impact surface was represented as a rigid volume and contact was through a spherical envelope centred on the outermost node of the crush can SBE (Figure 11).

5.5. Boundary conditions

Nodal boundary conditions represent the impact conditions with appropriate degrees of freedom constrained to ensure axial collapse (Figure 12).

5.6. Baseline response – MEM vs FEM

The force-time history showed several discrepancies when compared to FEM (Figure 13):

- MEM predicts a more gradual deceleration (0–6ms), suggesting a lower crush can stiffness;
- Mean crush force in the first crush can SBE occurs at the expected value of 137.6kN. However, subsequent SBEs present an increased mean crush force ~145kN
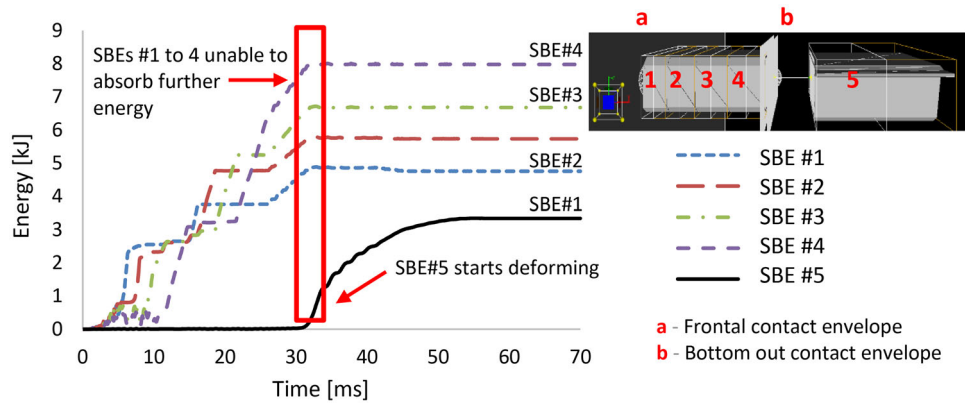
Figure 14. Strain Energy time histories for individual SBEs. After 32 ms, the crush can bottoms out, resulting in collapse initiating in the Longitudinal Rail (SBE #5).
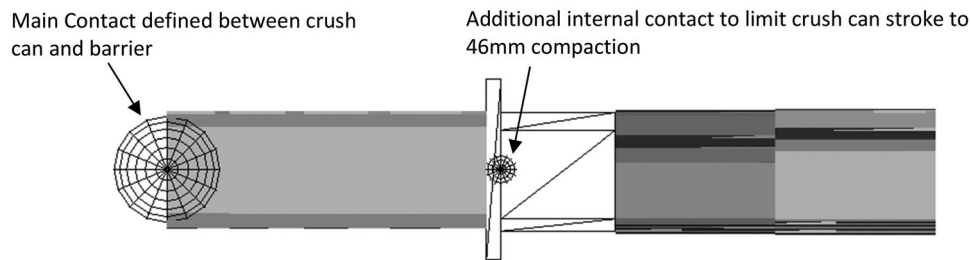

Figure 15. Additional internal contact pair required to align crush can stroke. When contact spheres interact, no further deformation possible (i.e. crush can becomes rigid).
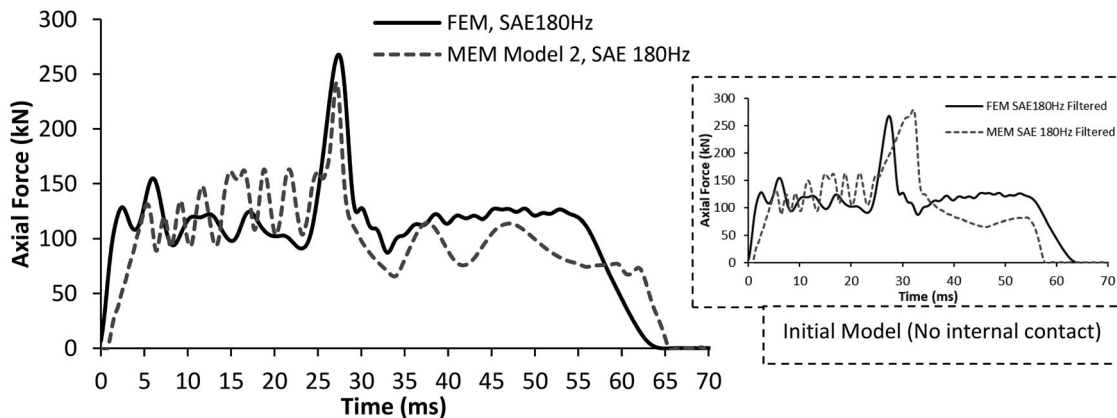

Figure 16. Modifying crush can collapse by introducing an internal contact to limit stroke and comparison to initial model with no internal contact.

(+5.1%), which is +10.3% larger than the 130kN design requirement;

- Bottoming out of the crash can occurs ~4.5ms later than FEM;
- MEM model comes to rest ~6.7ms earlier than FEM;

The strain energy time histories for each SBE show after ~12 ms, all SBEs representing the crash can are collapsing (Figure 14). This means consecutive triggers collapse sooner than expected, with stroke utilised after 32 ms (4.5 ms later than FEM). This indicated a mismatch in energy absorbed, with MEM crush can absorbing too much energy (~25 kJ), and longitudinal rail (~3 kJ), too little. Improvements were

therefore needed to correct the bottoming out response, trigger behaviour and discrepancies in longitudinal rail.

6. Improving MEM correlation – sensitivity studies

6.1. Modifying crush can collapse force – introducing internal contact

An additional internal contact was defined between SBE1 and 4 (Figure 15), to limit the compacted length to 46 mm predicted by FEM (Figure 8). This modification aligned peak collapse force in magnitude, duration and time of occurrence (27 ms) (Figure 16). Through strain energy

dissipation, 21 kJ and 7 kJ are now absorbed by crush can and longitudinal rail respectively (Figure 17). This finding demonstrates the need to have (a-priori) knowledge of the collapse mechanism (through test or high-fidelity simulation), to define internal contacts to limit deformation.

6.2. Influence of triggers

Two discrepancies are still present in Figure 16; the initial response (up to 6 ms) and post collapse behaviour of longitudinal assembly.

To understand the influence of triggers, lower and upper bound values were investigated (Figure 18). The upper bound response (no triggers) naturally brings the system to rest sooner, due to a greater amount of energy absorbed during formation of first peak. As trigger collapse force increases (from 140 kN to 220 kN), so too does crush can

stiffness. However, at higher trigger collapse forces (220 kN), the collapse sequence appears unphysical (Figure 19). Another unwanted consequence is the oscillatory nature in force-time histories (post 56 ms) when comparing 140 and 220 kN results, which was attributed to SBEs losing orientation when collapse occurs at multiple elements/locations.

To conclude, the discrepancy in initial stiffness (as influence of armature and exact geometry not considered) could not be solely be compensated through triggers. Lowering the triggering force to the mean collapse design requirement yields good agreement in terms of collapse sequence (energy absorbed) and time to bring the complete system to rest (MEM = 62.5 ms vs. FEM = 64.0 ms). Further work could investigate reducing the number of SBE and tuning triggers to provide closer alignment, but for this paper, this compromise was acceptable.

6.3. Longitudinal rail – influence of SBE discretisation

In the initial model, the longitudinal rail was represented with a single SBE. However, due to collapse and buckling observed from FEM, this required a minimum of two SBEs to allow for a plastic hinge to occur at some distance along its length.

Force-time comparisons between 30 and 75 ms for one and two SBEs are presented in Figure 20. In terms of time to bring the system to rest, there was a 3% error relative to FEM. The mean crush force for one/two SBE models are comparable, with a higher energy absorbed predicted by the two SBE variant (and closer to FEM). As expected, two SBEs show better geometric correlation to predicted collapse
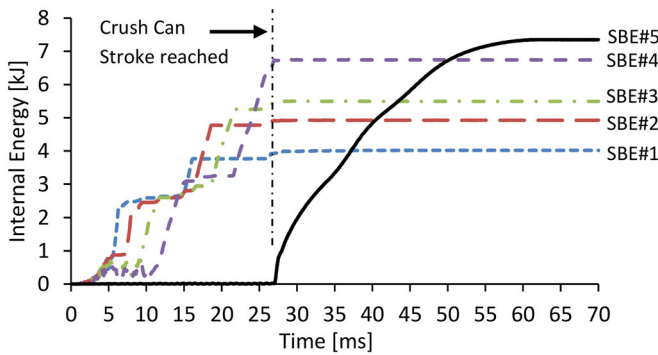

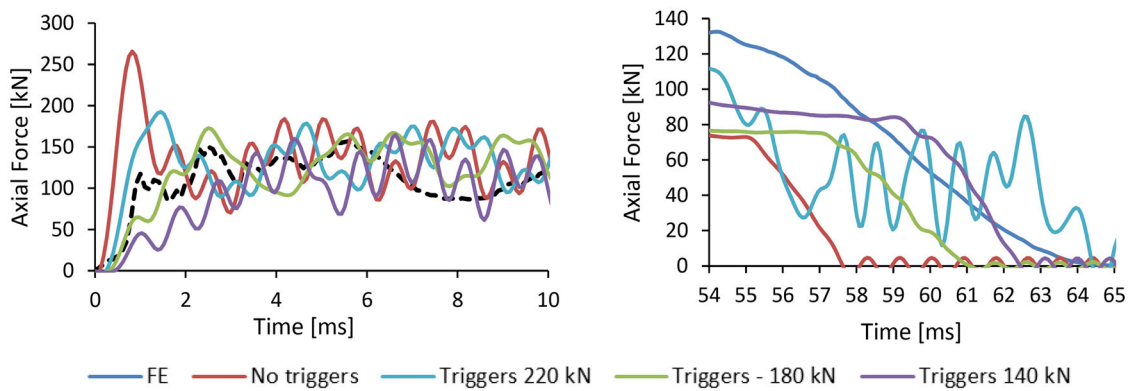**Figure 17.** Modified strain energies through introduction of internal crush can contact.

Figure 18. Influence of Trigger collapse on initial (<10ms) and post (54–65ms) CMS response.
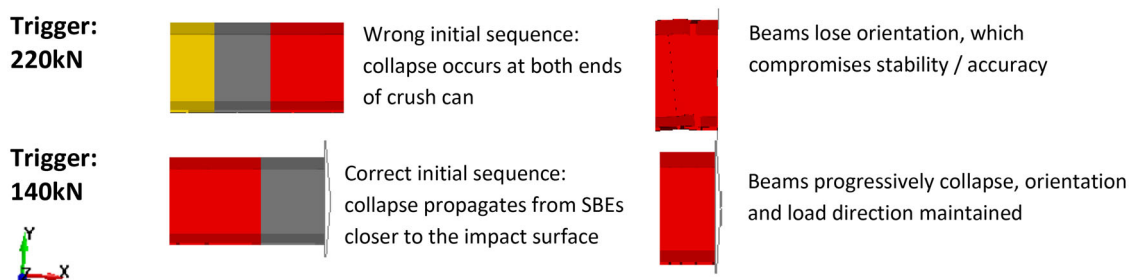

Figure 19. Influence of Trigger definition on Crush can collapse (yellow indicates post collapse, red deep collapse, grey is elastic).

mode with two distinct states of post and deep collapse, versus a single deep collapse state with one SBE (Figure 21).

As general guidance, SBE discretisation is determined by three factors:

i. Ensuring the length of the SBE is larger than the minimum plastic folding length;
ii. As SBE nodes act as interfaces, partition of SBE is required between connections of two or more beam cross-sections (or varying cross-sections), or at structural connections;
iii. To align MEM to test (or historical FEM of a similar vehicle variant), requires an a-priori understanding of the collapse mechanism, to allow different collapse states to exist along the length of a component (and is a similar historical challenge encountered with other hybrid methods, such as DRI-KRASH, etc.).

7. Final MEM vs FEM assessment: Automotive frontal crash management system

The final MEM model consisted six SBEs, two SolBEs (for rigid components) and two rigid contact envelopes and summarised, including computational resources in Table 8.

Comparing force-time histories in Figure 22, MEM predicted duration and key features of collapse and differentiated between post and deep collapse states. MEM overestimated mean crush and peak collapse force, but the mean relative difference remains within 15% (acceptable).

The onset of longitudinal rail collapse (and corresponding reduction in force) is predicted by MEM, which deviates after 40 ms, as MEM underestimates the load carrying
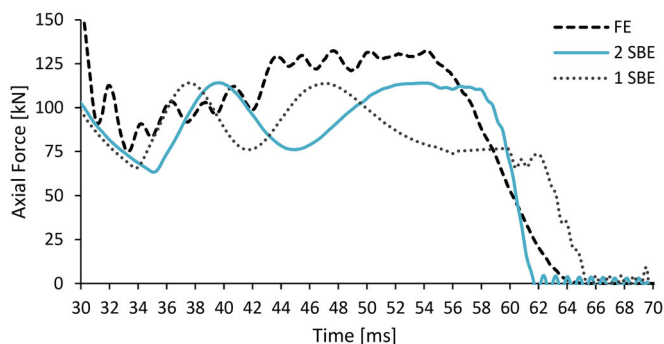
capability (which is not unexpected, as contact non-linearities and failure influenced FEM post rail collapse). Level of MEM agreement is extremely good, particularly considering the significant reduction in analysis time (Table 8).

8. Full vehicle case study

The frontal crash management system was isolated from a full vehicle OEM high fidelity model. To provide a more complex case study, the proposed framework was extended to the complete vehicle and analysed against a full barrier impact at 56 km/hr. The FE model consisted 3,455 components and 3 M elements, taking 16 h 30 mins to run on a single processor for comparative purposes to MEM.

This section compares three frontal structure variants against full-vehicle FEM, to assess influence of wheels and auxiliary systems (cooling pack) on the crash response:

i. Baseline BIW
ii. Baseline BIW + Wheels
iii. Baseline BIW + Wheels + Cooling Pack

8.1. Baseline full vehicle MEM model

To identify key energy absorbing components, several high-fidelity sub-assemblies were analysed to justify idealisation choices and check model stability, before integration into full vehicle MEM. For example:

a. Influence of a foam filled bumper and associated plastic components were neglected as these components primarily benefit load speed impacts. This simplification removed complications arising from additional tuned contact pairs to represent their response.
b. Bonnet also neglected, as once it buckles, its contribution to energy absorption is minimal. Constructed from

Figure 20. Influence of number of SBE used for Longitudinal Rail discretisation ($t = 30$ to 70 ms).

Table 8. Computation resources requried: FEM vs MEM.

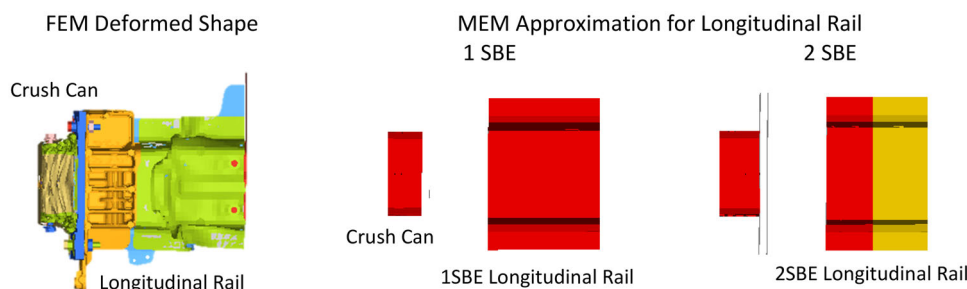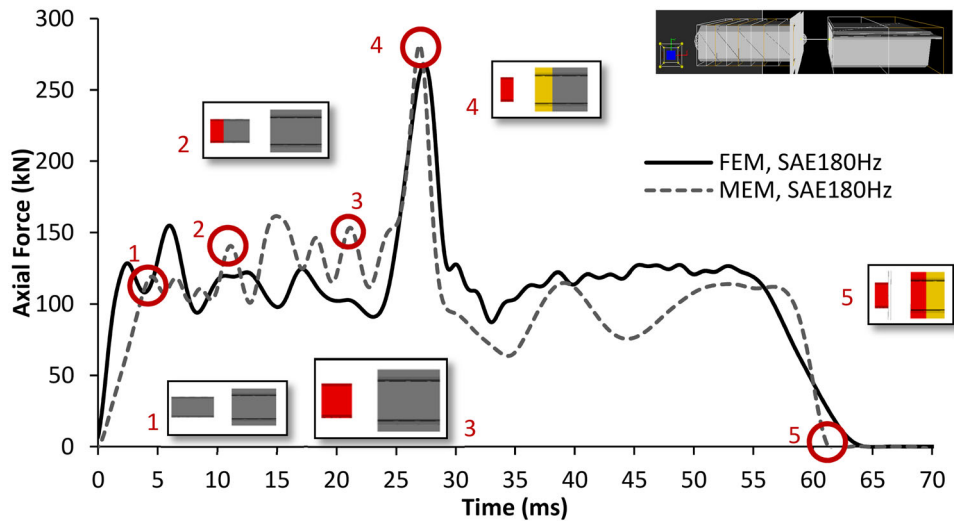|	FEM	MEM
Components / Features	96	10
Nodes	213,384	9
Materials	245	4
Run time	1h 21 min	3 seconds
Intel i7 @2.8GHz, 16Gb Ram	(8CPUs, mass scaling: $\Delta t = 0.8\mu s$)	(1CPU)

Figure 21. Longitdinal rail collapse as a function of SBEs (yellow indicates post collapse, red deep collapse).

Figure 22. Correlation between FEM and MEM for the frontal Crash Management System (SAE 180 Hz).

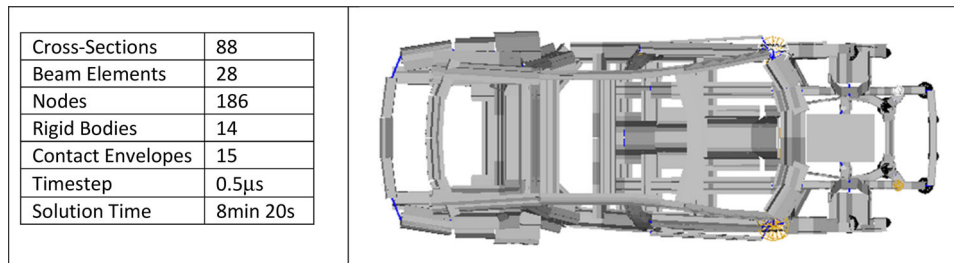|	
Cross-Sections	88
Beam Elements	28
Nodes	186
Rigid Bodies	14
Contact Envelopes	15
Timestep	0.5μs
Solution Time	8min 20s

Figure 23. Baseline MEM Model including key BIW components (no wheels, bonnet or cooling unit).

a thin metallic skin with underling frame and lattice reinforcement, this assembly could be represented by SBE with tuned sections. However, idealisation would be complex, requiring multiple contact envelopes, which could affect solution stability.

A summary of the model is presented in Figure 23, which contained key BIW components (Table 9).

The deformation sequence for the OEM full vehicle is provided in Table 10 and comparison between force-time histories in Figure 24.

The Baseline MEM model is capable of capturing key features of collapse. However, structural damage appears more severe, which may be due to sub-assemblies in the front part of the structure being neglected. From Figures 24 and 25, the following differences were observed:

1. During Stage 1, FEM predicted a more gradual deceleration (<7ms), and absorbed more energy with higher forces predicted ($10 < t < 30$ms). MEM predicts a stiffer initial response, as only key BIW components represented.
2. In Stage 2, MEM predicts two peaks (30 and 45ms). The first peak is due to engine impact with transverse dash beams, followed by engine impact with the barrier (45ms), which occurs slightly later than FE (38ms).
3. During Stage 3, both models predict the same features, with damage in the longitudinal transmission tunnel and forward transverse floor cross-beams.

4. In Stage 4 ($\sim$82ms), MEM predicts a third force peak, due to deformation occurring in the roof (not predicted by FEM).

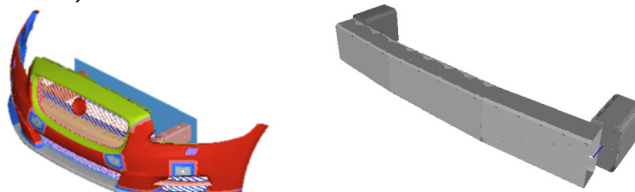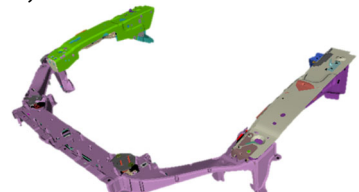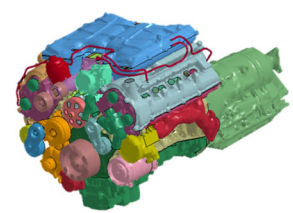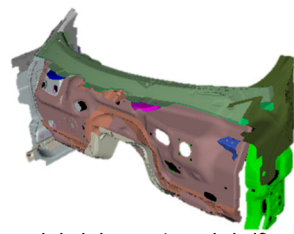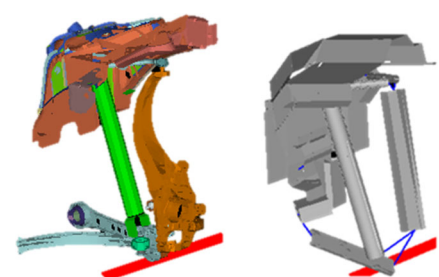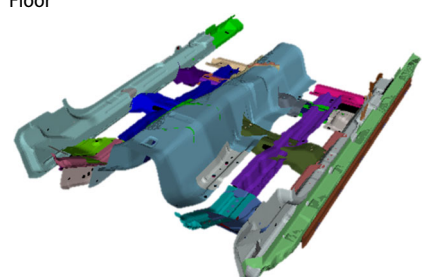## 8.2. Baseline full vehicle MEM model: Influence of wheels

Wheel response during a frontal load path provides an additional load path that directly loads the lower A-pillar once wheel compaction occurs.

Wheel response is complex and highly non-linear due to its mixed material construction and its response was investigated by compressing a pressurised tyre between two rigid walls at $10 \, \text{ms}^{-1}$ (Figure 26a). MEM representation resembled wheel dimensions and its behaviour represented by a user-defined contact function. An acceptable response was achieved with a 70 kN/m contact stiffness and deemed sufficient to assess tyre influence on vehicle response (Figure 26b). (However, it is acknowledged wheel modelling using tuned SBEs would be an area for further investigation).

Wheel inclusion is critical during a frontal impact, due to an improved alignment with FEM:

1. MEM response is closer aligned in Stage 1. With additional energy absorption and load path provided through the wheels, peak forces between engine and dash beams lowered.

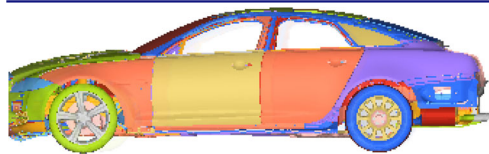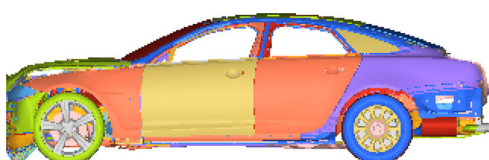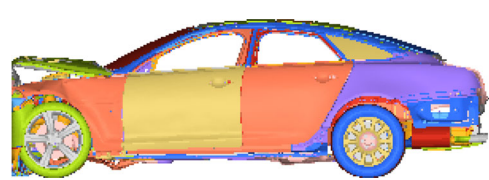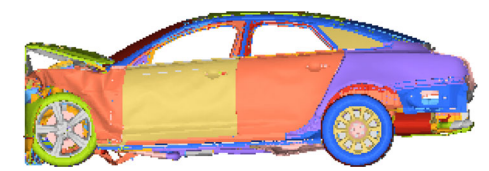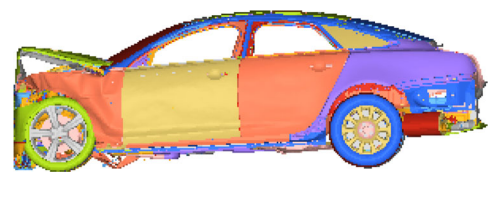**Table 9.** Key BIW components and MEM idealisations – Baseline Full Vehicle Model.

Bumper Assembly

Only transversal beam, crush can and connection to longitudinal lower S-Rails included. (Foam and plastic parts neglected)

Engine

The 375kg engine can be considered non-deformable, with representative CoG and inertia properties assigned to a rigid volume, connected to the supporting structure through solid beams.

Shock Towers

Form a major structural connection between wheels and lower and upper sub-frames.

Upper Engine Bay Frames

Secondary lateral beams, which supports bonnet, bumper and contributes to chassis stiffness.

Firewall

Fire Wall, horizontal dash beams (parcel shelf) and lower side pillars contributes significantly to torsional stiffness and separates engine bay from passenger compartment

Passenger Floor

Consists transmission Tunnel, longitudinal and lateral floor beams.

2. Load path through lower A-pillar and underfloor longitudinal beams improved correlation during later stages of collapse (Stage 3). Damage in upper roof structure removed.
3. There is a 5ms difference in duration of collapse sequence (FEM 97.5ms vs 101.5ms MEM).
4. From Figure 27, deep collapse predicted in lower side frame and forward underfloor cross-beams (and more severe than FEM). This problem was a consequence of rigid contact envelopes penetrating, which instead of a gradual decrease in penetration during rebound, an instantaneous unloading occurs, resulting in increased (artificial) structural damage.

8.3. Baseline full vehicle MEM model: Influence of cooling unit

The auxiliary frontal cooling systems was represented by a single contact envelope attached to the power train with a user defined stiffness of 200 kN/m identified as being representative from sub-modelling. Kinematics and force-time comparisons are presented in Figures 28–30.

1. Representing additional energy absorbing components is beneficial, as addition of wheels and cooling system provides close correlation to FEM, with an average relative error of ±10.65% and a Pearson's correlation coefficient of 0.96.
2. Incorporating secondary energy absorbing components tends to decrease model instabilities and reduces failure of SBEs due to high force peaks.
3. MEM predicts increased damage to underfloor structure (longitudinal transmission tunnel and aft transverse cross-beams), which is not predicted by FEM.
4. Contact envelope locking in the wheel (and increased lower side frame damage) is not evident in this model, as nearside wheel momentarily changes direction, avoiding the previous problem of instantaneous (and artificial) unloading. This finding suggests how critical the importance of representative wheel modelling during a frontal impact.
5. For comparative assessment, solution on a single processor (2.4GHz, 8Gb RAM) was 7.5mins for MEM and 16.5hrs for FEM. The longer MEM runtime is due to choosing a small explicit solution timestep (1µs) to overcome solution instabilities.

Table 10. Deformation Sequence (High Fidelity FEM) at 56 km/hr onto a full barrier.

7ms:

- Bumper and foam fully compressed

25ms:

- Crush can stroke fully utilised
- Bonnet buckles

38ms:

- Maximum force reached due to engine contact with barrier.
- Gear box supports fail, no damage to chassis.
- Front sub-frame starts deforming (buckling).
- Wheels pushed rearward and contact fender walls.

65ms:

- Second force peak due to engine colliding with fire wall.
- Plastic deformation noticeable on transmission tunnel.
- Wheels bottom out and loads lower A-Pillar.

90–100ms:

- Kinetic Energy of impact fully absorbed
- No passenger cell intrusion, or severe distortion.
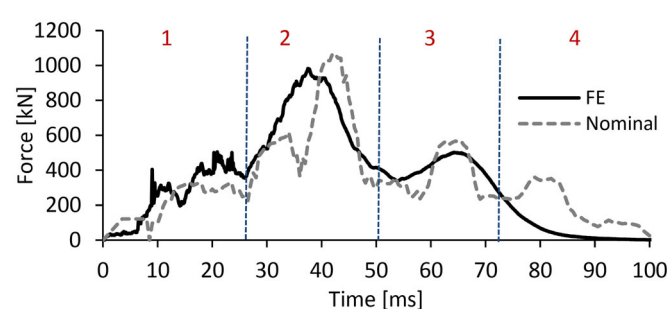- Vehicle rebound from barrier initiates.

Figure 24. Correlation between FEM and MEM for Nominal Model (SAE 180 Hz).

9. Conclusions

- This paper discusses a MEM modelling framework for development of robust and accurate equivalent MEM models, based on abstraction from high fidelity finite element models.
- To align MEM to test (or historical FEM of a similar vehicle variant), requires an a-priori understanding of the collapse mechanism.
- Model complexity reduction (abstraction) is based on hierarchical modelling that typically involves several levels of detail, enabling identification of components that can be neglected, or components to be represented
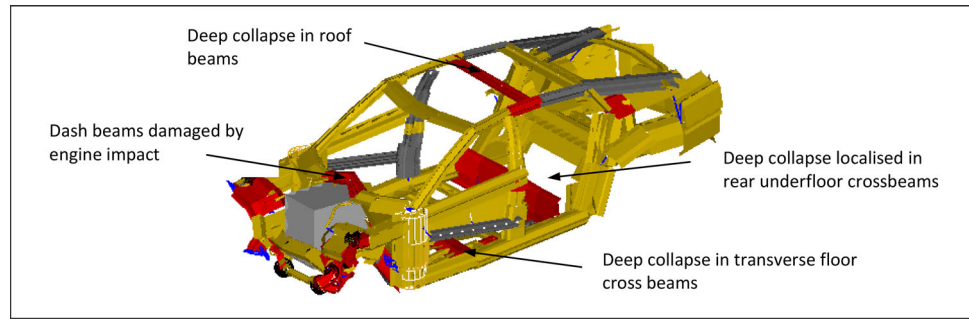

Figure 25. Nominal MEM model for final deformed shape at 56 km/hr impact onto a frontal barrier.
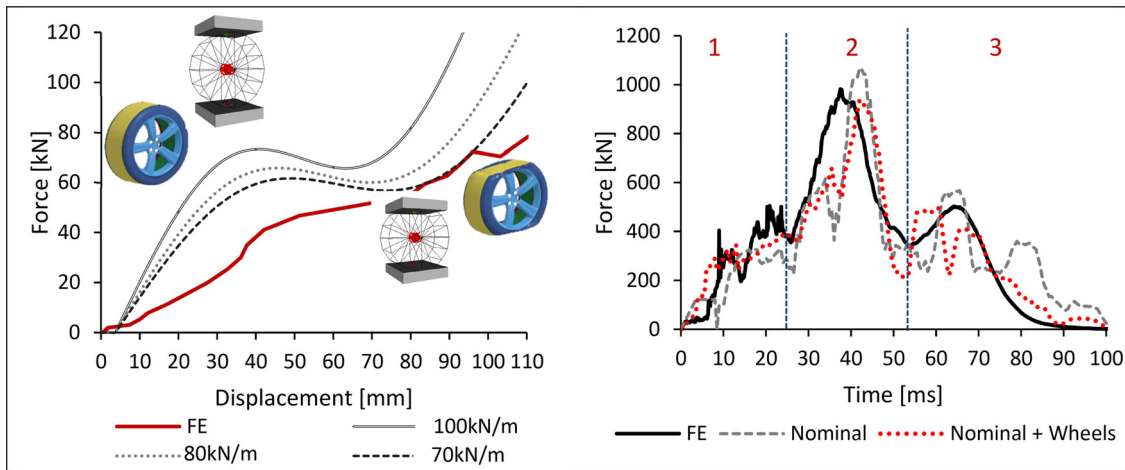
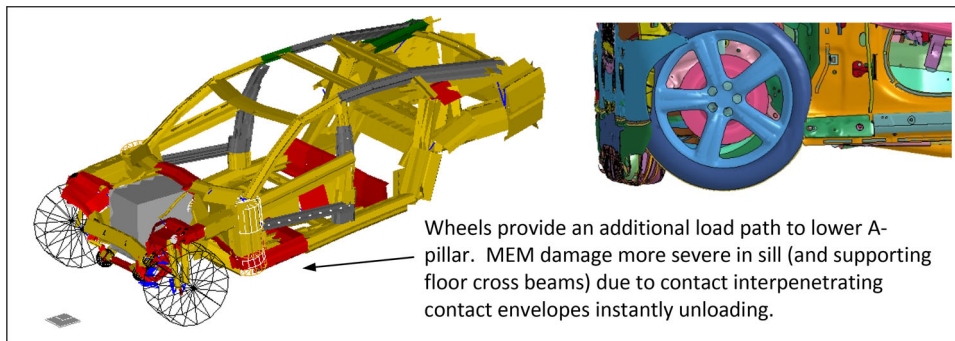**Figure 26.** (a) Representation of compressive wheel MEM response and (b) Influence on full-vehicle response.

Wheels provide an additional load path to lower A-pillar. MEM damage more severe in sill (and supporting floor cross beams) due to contact interpenetrating contact envelopes instantly unloading.

Figure 27. Influence of wheels on collapse response during a 56 km/hr impact onto a frontal barrier.
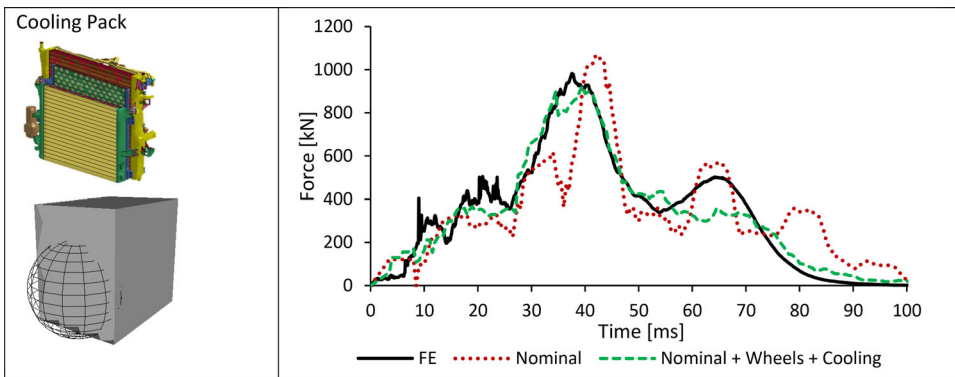
Figure 28. FE and VCS Nominal + wheels + Cooling Pack frontal impact comparison.

Deep collapse in dash beams

Increased damage predicted in transverse underfloor beams.

Contact problem (and artificial damage) in lower side frame removed due to nearside wheel changing direction
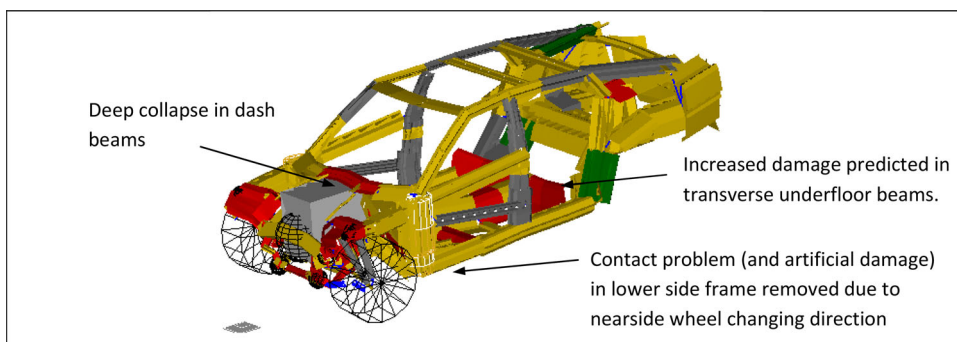
Figure 29. Inclusion of Wheels and Cooling Assembly provides good correlation to FEM.

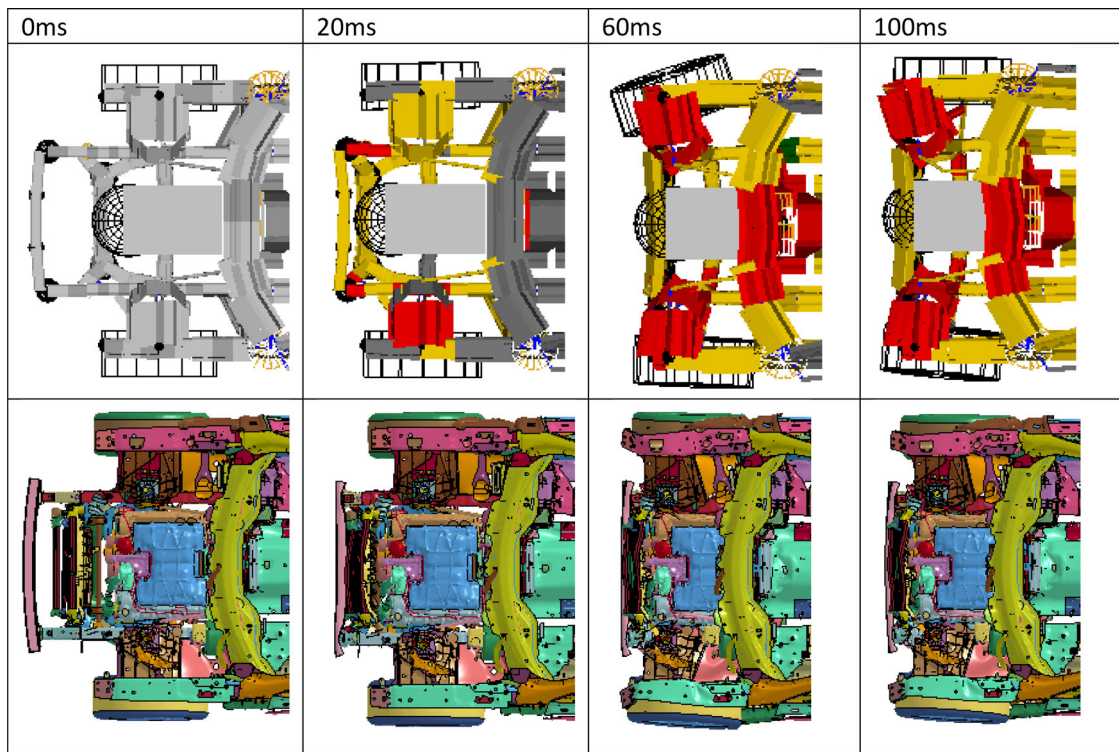| 0ms	20ms	60ms	100ms

Figure 30. Deformation comparison as viewed from underneath vehicle.

through tuned, user defined contact pairs. Internal (rigid) contacts are recommended to align component stroke.

For instance – For full vehicle barrier impact, inclusion of wheels and auxiliary cooling system *via* tuned contact stiffnesses, represented the load path through the vehicle, with key features predicted and an average relative error within ±10% across the force-time history, with a significant reduction in run time (7.5 mins vs 16.5 hrs for FEM).

- The more complex the MEM, the more likely are solution instabilities (which are time consuming to debug). Solution convergence can be improved by following the recommendations below:

  - Model cross-sections with minimum number of points (i.e. avoid over defining);
  - Ensure the length of an SBE is larger than the minimum plastic folding length;
  - As SBE nodes act as interfaces, partitioning required where cross-sections vary, where hinge formation may occur, or at structural connections.
  - Merging critical Super Beam Elements to minimise contact envelope penetration;
  - Reduce the number of contact envelopes to a minimum. For critical contacts, the contact radius is a user-defined parameter and requires tuning
  - Reducing the explicit timestep to order of microseconds to aid convergence
- Triggers need careful consideration to prevent unrealistic collapse at multiple locations (i.e. not progressive or sequential). Collapse at multiple locations causes accuracy and stability issues due to SBE losing orientation.

- MEM offers significant advantages in supporting vehicle design and offers considerable potential to support design space exploration across multiple crash certification cases.

For example, the ten component MEM frontal crash system impacting a rigid barrier at 8.6 m/s, predicted duration (62.5 ms vs. 64.0 ms -FEM), key features of collapse and differentiated between post and deep collapse states. With a solution time of 3 secs, MEM achieved an average relative error of ±15% across the force-time history when compared to FEM.

Acknowledgements

Disclosure statement

No potential conflict of interest was reported by the authors.

ORCID

Kevin Hughes http://orcid.org/0000-0002-8522-7903

References

[1] Schauwecker F, Moncayo D, Beck M, et al. Investigation of the failure behaviour of bolted connections under crash loads and a novel adaption to an enhanced abstracted bolt model. In *15th International LS-DYNA Users Conference – Connections*, Detroit, MI, 2018.

[2] Cafolla J, Hall R, Norman D, et al. Forming to crash simulation in full vehicle models. In *4th European LS-DYNA Users Conference – Metall Forming II*, Ulm, Germany, 2003.

[3] Andrade F, Feucht M. Failure prediction in crash simulations with the GISSMO model. In *LS-DYNA Forum 2018*, Bamberg, Germany, 2018.

[4] Heibel S, Nester W, Clausmeyer T, et al. Influence of different yield loci on failure prediction with damage models. J Phys: Conf Ser. 2017;896:012081.

[5] Alexander J. An approximate analysis of the collapse of thin cylindrical shells under axial loading. Q J Mech Appl Math. 1960;13(1):10–15.

[6] Abramowicz W. The effective crushing distance in axially compressed thin-walled metal columns. Int J Impact Eng. 1983;1(3):309–317.

[7] Abramowicz W, Jones N. Dynamic axial crushing of circular tubes. Int J Impact Eng. 1984;2(3):263–281.

[8] Abramowicz W, Jones N. Dynamic progressive buckling of circular and square tubes. Int J Impact Eng. 1986;4(4):243–270.

[9] Wierzbicki T, Bhat S. A moving hinge solution for axisymmetric crushing of tubes. Int J Mech Sci. 1986;28(3):135–151.

[10] Wierzbicki T, Recke L, Abramowicz W, et al. Stress profiles in thin-walled prismatic columns subjected to crush loading-I. Compression. Comput Struct. 1994;51(6):611–623.

[11] Wierzbicki T, Recke L, Abramowicz W, et al. Stress profiles in thin-walled prismatic columns subjected to crush loading II: Bending. Comput Struct. 1994;51(6):625–641.,

[12] Takada K, Abramowicz W. Macro element fast crash analysis of 3D space frame. SAE Technical Paper 2007-01-0894, 2007..

[13] Georgiou G, Zeguer T. On the assessment of the macro-element methodology for full vehicle crashworthiness analysis. Int J Crashworthiness. 2018;23(3):336–353.

[14] Pyrz M, Krzywoblocki M. Crashworthiness optimization of front rail structure using macro element method and evolutionary algorithm. Struct Multidisc Optim. 2019;60(2):711–726.

[15] Livermore Software Technology Corporation (LSTC), LS-DYNA, R10.0, October 2017.

[16] Impact Design Europe, Visual Crash Studio (VCS) – V.4.0, Poland, 2017.

[17] Impact Design Europe, Crash Academy / Publications, 2018. [Online]. Available from: http://impactdesign.pl/crash-academy/.

[18] Abramowicz W. Chapter 1: The macro element method in crashworthiness calculations [Online]. Available from: http://impactdesign.pl/wp-content/uploads/2016/03/CA_publications_05_VCS-full_description.pdf.

[19] Abramowicz W. Thin-walled structurs as impact energy absorbers. Thin-Walled Struct. 2003;41(2-3):91–107.

[20] Abramowicz W. An alternative formulation of the FE method for arbitrary discrete/continuous models – Object Orientation Formulation, Impact Design Europe, http://impactdesign.pl/wp-content/uploads/2016/03/CA_publications_01_ObjectOrientedFormulation.pdf.

[21] Witteman WJ. *Improved vehicle crashworthiness design by control of the energy absorption for different collision situations*, Doctoral Dissertation. Eindhoven University of Technology: 1999.

[22] Abramowicz W, Jones N. Dynamic axial crushing of square tubes. Int J Impact Eng. 1984;2(2):179–208.

[23] Mahmood H, Paluszny A. Stability of plate-type box columns under crush loading. In Computational methods in ground transportation vehicles, Phoenix, AR, American Society of Mechanical Engineers – Winter Meeting, 1982. pp. 17–33.

[24] National Institute of Mental Health, ImageJ – Image Processing and Analysis in Java [Online]. Available from: https://imagej.nih.gov/ij/.